Since January 2020 Elsevier has created a COVID-19 resource centre with free information in English and Mandarin on the novel coronavirus COVID-19. The COVID-19 resource centre is hosted on Elsevier Connect, the company's public news and information website.

Journal of Molecular Structure 1253 (2022) 132242

Contents lists available at ScienceDirect

Journal of Molecular Structure

journal homepage: www.elsevier.com/locate/molstr

Synthesis and investigation of anti-COVID19 ability of ferrocene Schiff base derivatives by quantum chemical and molecular docking

Ghulam Abbas[a,*], Ahmad Irfan[b,c], Ishtiaq Ahmed[d], Firas Khalil Al-Zeidaneen[e], S. Muthu[f], Olaf Fuhr[g], Renjith Thomas[h]

[a] Institute of Inorganic Chemistry, Karlsruhe Institute of Technology, Engesserstrasse 15, 76131 Karlsruhe, Germany
[b] Research Center for Advanced Materials Science, King Khalid University, P.O. Box 9004, Abha 61413, Saudi Arabia
[c] Department of Chemistry, College of Science, King Khalid University, P.O. Box 9004, Abha 61413, Saudi Arabia
[d] Department of Chemical Engineering and Biotechnology (CEB) Philippa Fawcett Drive, University of Cambridge, Cambridge CB3 0AS, UK
[e] Department of Chemistry and Chemical Technology, Tafila Technical University, Tafila, Jordon
[f] Department of Physics, Aringnar Anna Govt. Arts College, Cheyyar, 604407, Tamilnadu, India
[g] Institute of Nanotechnology, Karlsruhe Institute of Technology, Hermann von-Helmholtz Platz 1, 76344 Eggenstein-Leopoldshafen, Germany
[h] Department of Chemistry, St Berchmans College (Autonomous), Changanassery, Kerala, India

ARTICLE INFO

Article history:
Received 11 October 2021
Revised 3 December 2021
Accepted 19 December 2021
Available online 24 December 2021

Keywords:
Ferrocene derivatives
Anti-COVID19
Molecular docking
Molecular descriptors

ABSTRACT

The recent outbreak of coronavirus disease (COVID-19) has rampaged the world with more than 236 million confirmed cases and over 4.8 million deaths across the world reported by the world health organization (WHO) till Oct 5, 2021. Due to the advent of different variants of coronavirus, there is an urgent need to identify effective drugs and vaccines to combat rapidly spreading virus varieties across the globe. Ferrocene derivatives have attained immense interest as anticancer, antifungal, antibacterial, and antiparasitic drug candidates. However, the ability of ferrocene as anti-COVID-19 is not yet explored. Therefore, in the present work, we have synthesized four new ferrocene Schiff bases (L1-L4) to understand the active sites and biological activity of ferrocene derivatives by employing various molecular descriptors, frontier molecular orbitals (FMO), electron affinity, ionization potential, and molecular electrostatic potential (MEP). A theoretical insight on synthesized ferrocene Schiff bases was accomplished by molecular docking, frontier molecular orbitals energies, active sites, and molecular descriptors which were further compared with drugs being currently used against COVID-19, i.e., dexamethasone, hydroxychloroquine, favipiravir (FPV), and remdesivir (RDV). Moreover, through the molecular docking approach, we recorded the inhibitions of ferrocene derivatives on core protease (6LU7) protein of SARS-CoV-2 and the effect of substituents on the anti-COVID activity of these synthesized compounds. The computational outcome indicated that L1 has a powerful 6LU7 inhibition of SARS-CoV-2 compared to the currently used drugs. These results could be helpful to design new ferrocene compounds and explore their potential application in the prevention and treatment of SARS-CoV-2.

1. Introduction

The outbreak of coronavirus disease (COVID-19) in Wuhan city of China in December 2019 was renamed severe acute respiratory syndrome coronavirus 2 (SARS-CoV2) by the international committee on taxonomy [1]. Due to its rapid human-to-human transmission, the world health organization (WHO) declared COVID-19 as a pandemic on 12 March 2020 [2]. According to WHO, SARS-CoV2 has rampaged the world with more than 236 million confirmed cases and over 4.8 million deaths across the world till Oct 5, 2021. In last week, the highest numbers of new cases were reported due to new variant of virus in India (70%) [3]. Public health has been affected the most because people do not have the opportunities to access a modern health system and medicine in developing countries of Africa, Latin America and the Caribbean [4,5]. Due to different variants of the coronavirus, there is an urgent need to identify effective drugs and vaccines to combat rapidly spreading virus varieties across the globe [6].

Ferrocene derivatives have attained immense interest as anticancer, antifungal, antibacterial, and antiparasitic drug candidates [7]. Ferrocene was used for the treatment of anemia in the former USSR because of its low toxicity [8]. The lipophilicity of ferrocenyl groups allows ferrocene, to be administered orally for the treatment of gum diseases which is not the case for simple Fe(II)

* Corresponding author.
E-mail address: ghulam.abbas@kit.edu (G. Abbas).

https://doi.org/10.1016/j.molstruc.2021.132242
0022-2860/

salts [9]. Furthermore, the activity of ferrocene compounds towards cancer was first investigated in 1978. This early work involved the synthesis of new compounds bearing an antigen that binds strongly to nucleic acids [10]. A ferrocenyl group was chosen as the antigenic moiety, which demonstrated that ferrocenyl polypeptides elicit a strong antigenic response [11]. Thus the ferrocene-based drugs have a marked effect on molecular properties e.g. redox activation and lipophilicity. Moreover, ferrocene compounds containing alcohol substituents have proved to be versatile precursors for effective anticancer and antimalarial agents [12–14].

In the present work, we have synthesized ferrocene derivatives (**L1-L4**) and characterized them by NMR spectroscopy and Mass spectrometry. The compound **L4** was further characterised by single-crystal diffraction. Moreover, we have demonstrated the inhibition impact of ferrocene derivatives over SARS-CoV-2, providing an essential base for the resistance of ferrocene compounds against prime protease (6LU7) proteins of SARS-CoV-2 through docking simulations. We further highlighted the molecular descriptors, ionization potential (IP), frontier molecular orbitals (FMO), electron affinity (EA), and molecular electrostatic potential (MEP) analysis to explore the biological and pharmacological activities. The electronic characteristics along with global reactivity descriptors including electrophilicity index (ω), electronegativity (χ), chemical potential (μ), softness (S) as well as chemical hardness (η) were carried out to understand the active sites of ferrocene derivatives. The outcome of the work demonstrated that the synthesized ferrocene derivatives have an appreciable ability to inhibit SARS-CoV-2 invasion within the human body.

2. Experimental

2.1. Materials

Ferrocenecarboxaldehyde, 2-amino-4-chlorophenol, 2-amino-4-phenylphenol, 2-amino-4-nitrophenol, and 2-amino-4-sulfony lphenol were purchased from Acros Organics (Geel, Belgium). All chemicals and solvents were of analytical grade and used as received. All reactions were carried out under aerobic conditions.

2.2. Instrumentation

The elemental analysis (C H N) was performed using an Elementar Vario EL analyzer. Fourier transform IR spectra were measured on a Perkin–Elmer Spectrum One spectrometer with samples prepared as KBr discs. UV–Vis absorption spectroscopy of synthesized samples was carried out by Varian Cary 500 Scan UV–VIS NIR Spectrophotometer. Solution NMR spectra were recorded with Bruker Avance instruments operating at ^{1}H Larmor frequencies of 400 MHz, using DMSO–d_6 as solvent and TMS as an internal standard for ^{13}C and ^{1}H nuclei.

2.3. X-ray crystallography

A single crystal of the **L4** with dimensions of 0.24 × 0.2 × 0.03 mm was mounted in a glass capillary and data were collected on a Stoe StadiVari diffractometer. Intensity data were collected with graphite monochromated Ga Ka radiation (λ = 1.34143 nm) at 150 K. The structure was solved by direct methods using SHELXLS-2015 and refined against F^2 by full matrix least squares using SHELXL-2015 [15]. A summary of pertinent crystal data, experimental details and refinement results are shown in Table 1. Crystallographic data for complex have been deposited with the Cambridge Crystallographic Data Center, CCDC No. 2,081,830. Copies may be obtained free of charge from www.ccdc.cam.ac.uk/conts/retrieving.html or from the CCDC, 12 Union Road, Cambridge, CB2 1EZ, UK (email: deposit@ccdc.cam.ac.uk).

Table 1
Crystal data and refinement parameters of L4.

Empirical formula	$C_{17}H_{14}ClFeNO$
Formula weight	339.59
Temperature/K	150
Crystal system	monoclinic
Space group	$P2_1/n$
a/Å	13.1760(7)
b/Å	17.2007(9)
c/Å	13.4953(8)
α/°	90
β/°	109.467(4)
γ/°	90
Volume/Å^3	2883.7(3)
Z	8
ρ_{calc}g/cm^3	1.564
μ/mm^{-1}	6.752
F(000)	1392.0
Crystal size/mm^3	0.24 × 0.2 × 0.03
Radiation	GaKα (λ = 1.34143)
2Θ range for data collection/°	7.066 to 128.536
Index ranges	$-17 \le h \le 15$, $-16 \le k \le 22$, $-17 \le l \le 14$
Reflections collected	22,138
Independent reflections	7034 [R_{int} = 0.0555, R_{sigma} = 0.0923]
Data/restraints/parameters	7034/0/381
Goodness-of-fit on F^2	0.924
Final R indexes [$I>=2\sigma$ (I)]	R_1 = 0.0547, wR_2 = 0.1271
Final R indexes [all data]	R_1 = 0.1183, wR_2 = 0.1491
Largest diff. peak/hole / e Å^{-3}	0.57/−0.65

2.4. Synthesis of ferrocene derivatives

2.4.1. Synthesis of N-(2–hydroxy-5-biphenyl) ferrocylideneamine (L1)

Ferrocencarboxaldehyde (1.07 g, 5 mmol) and 2-amino-4-phenylphenol (0.927 g, 5 mmol) were dissolved in 20 mL of ethanol (absolute) and the mixture was refluxed for 3 h. The reaction mixture was cooled to room temperature and left overnight to afford brown precipitates. The product was further purified by recrystallization in dichloromethane. FT-IR (KBr cm−1) 3166, 3075 and 2969 (C–H str), 1596.34 (C = N str), 1101.60, 1080.43 (Ar–CH), 468.17, 488.77 cm^{-1} (Cp C–H). UV–Vis ($CHCl_3$) λ_{max} 238, 261, 358, and 460 nm. ^{1}H NMR (DMSO–d_6, 400 MHz) δ (ppm): 4.32 (s, 5H, Fc-unsubstituted ring), 4.69 (s, 2H, H-3, H-4, Fc-substituted ring), 4.82 (s, 2H, H-2, H-5, Fc-substituted ring), 6.45 (s, 1H, Ar-H), 6.54 (s, 1H, Ar-H), 6.70 (s, 1H, Ar-H), 6.89 (s, 1H, Ar-H), 7.24 (m, 1H, Ar-H), 7.37 (m, 2H, Ar-H), 7.50 (m, 2H, Ar-H), 8.49 (s, 1H, CH=N), 9.31 (bs, 1H, Ar-OH).

^{13}C NMR (DMSO–d_6, 100 MHz) δ (ppm): 69.88 (C-2, C-5, Fc-substituted ring), 69.91 (C-5, Fc-unsubstituted ring), 73.53 (C-3, C-4, Fc-substituted ring), 80.02 (C-1, Fc-substituted ring), 112.96 (Ar-CH), 115.30 (Ar-CH), 122.62 (Ar-CH), 126.33 (Ar-C-Cl), 129.10 (Ar-CH), 130.89 (Ar-CH), 132.62 (Ar-CH), 133.21 (Ar-CH), 135.17 (Ar-CH), 138.97 (Ar-C-N), 148.57 (Ar-C-OH), 165.93 (CH=N).

MS (EI) *m/z*: 381.09 (78.45%), 316.04 (47.55%), 289.04 (21.89%), 215.00 (66.72%), 214.00 (97.49%), 186.01 (100%), 170.06 (65.82%), 120.96 (96.71%).

2.4.2. Synthesis of N-(2–hydroxy-5-nitrophenyl) ferrocylideneamine (L2)

2-amino-4-phenylphenol is replaced with 2-amino-4-nirophenol in the procedure given in 2.3.1. FT-IR (KBr cm^{-1}) 3068 and 3023 (C–H str), 1592.88 (C = N str) 1104.97, 1073.68 (Ar–CH) 471.18, 493.18 cm^{-1} (Cp C–H). UV–Vis ($CHCl_3$) λ_{max} 237, 256, 299, 323 and 484 nm.

^{1}H NMR (DMSO–d_6, 400 MHz) δ (ppm): 4.30 (s, 5H, Fc-unsubstituted ring), 4.68 (s, 2H, H-3, H-4, Fc-substituted ring), 4.91

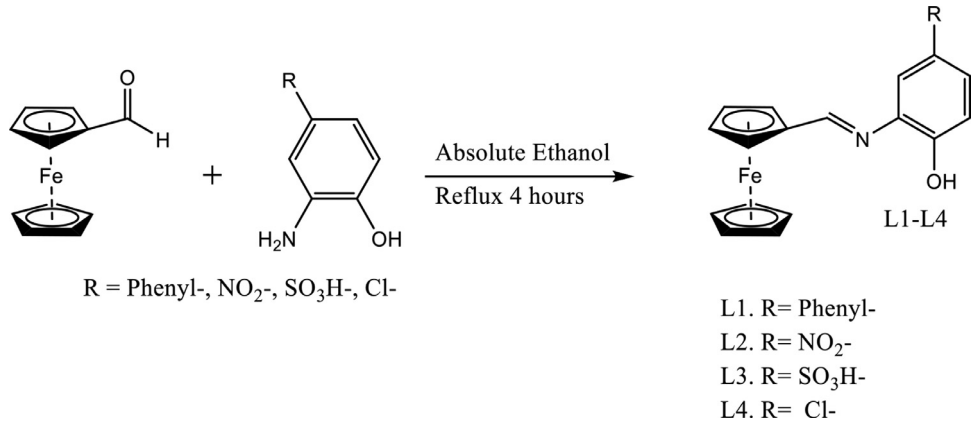

Scheme 1. Ferrocene Schiff base derivatives studied in the current work.

(s, 2H, H-2, H-5, Fc-substituted ring), 6.75 (d, J = 8.5 Hz, 1H, Ar-H), 7.37 (d, J = 8.5 Hz, 1H, Ar-H), 7.46 (s, 1H, Ar-H), 8.59 (s, 1H, CH=N), 9.36 (bs, 1H, Ar-OH).

^{13}C NMR (DMSO–d_6, 100 MHz) δ (ppm): 69.77 (C-2, Fc-substituted ring), 69.87 (C-5, Fc-substituted ring), 69.90 (C-5, Fc-unsubstituted ring), 73.52 (C-3, C-4, Fc-substituted ring), 79.88 (C-1, Fc-substituted ring), 108.11 (Ar-CH), 113.51 (Ar-CH), 113.58 (Ar-CH), 136.06 (Ar-C-NO_2), 140.04 (Ar-C-N), 151.13 (Ar-C-OH), 166.85 (CH=N).

MS (EI) *m/z*: 351.06 (74.10%), 350.06 (100.00%), 348.05 (46.00%), 320.07 (34.91%), 285.00 (37.80%), 186.011 (56.12%), 120.96 (61.90%).

2.4.3. Synthesis of N-(2–hydroxy-5-sulfonylphenyl) ferrocylideneamine (L3)

2-amino-4-phenylphenol is replaced with 2-amino-4-sulfonylphenol in the procedure given in 2.3.1. FT-IR (KBr cm^{-1}) 3380 and 3094 (C–H str), 1639 (C = N str) 1102, 1071 (Ar–CH) 461, 566 cm^{-1} (Cp C–H). UV–Vis ($CHCl_3$) λ_{max} 237, 268, 337 and 451 nm.

^{1}H NMR (DMSO–d_6, 400 MHz) δ (ppm): 4.29 (s, 5H, Fc-unsubstituted ring), 4.47 (s, 2H, H-3, H-4, Fc-substituted ring), 4.67–480 (m, 2H, H-2, H-5, Fc-substituted ring), 6.88 (d, J = 8.6 Hz, 1H, Ar-H), 7.40 (d, J = 8.6 Hz, 1H, Ar-H), 7.53 (s, 1H, Ar-H), 8.61 (s, 1H, CH=N), 9.34 (bs, 1H, Ar-OH).

^{13}C NMR (DMSO–d_6, 100 MHz) δ (ppm): 69.87 (C-2, Fc-substituted ring), 69.91 (C-5, Fc-substituted ring), 73.53 (C-5, Fc-unsubstituted ring), 73.61 (C-3, C-4, Fc-substituted ring), 79.87 (C-1, Fc-substituted ring), 115.43 (Ar-CH), 116.51 (Ar-CH), 119.21 (Ar-CH), 120.31 (Ar-CH), 140.8 (Ar-C-SO_3H), 141.02 (Ar-C-N), 150.06 (Ar-C-OH), 163.83 (CH=N).

MS (EI) *m/z*: 382.06 (35.13%), 322.66 (39.91%), 291.04 (41.81%), 213.95 (74.60%), 185.96 (57.57%), 120.94 (100%).

2.4.4. Synthesis of N-(2–hydroxy-5-chlorophenyl) ferrocylideneamine (L4)

2-amino-4-phenylphenol is replaced with 2-amino-4-cholorophenol in the procedure given in 2.3.1. The characterization of the compound has been reported previously [16].

2.5. Computational details

In biological systems, the density functional theory (DFT) is a fascinating method to analyze numerous important properties [17–20]. The DFT analysis has a significant contribution to the investigation of electronic characteristics of molecules [21–25] as well as optimize geometries within the ground state (S_0) [26,27]. B3LYP is a coherent functional for the S_0 geometries of numerous biologically active molecules. In current investigations regarding S_0 geometries optimizations as well as electronic characteristics, we adopted B3LYP/6–31G**(LANL2DZ) within Gaussian16 software [28]. Furthermore, Autodock version 4.2 was endorsed through Autodock MGL tools for docking by employing the strategy of eliminating H_2O followed by the addition of more polar hydrogen moiety. Autodock 4.2, the Autogrid resolute the native ligand location around the binding site by organizing the grid coordinates (X, Y, and Z-axis). The docking computations were executed with Autodock 4.2 along with Pymol version 1.7.4.5 Edu.

3. Results and discussion

3.1. Synthesis of ferrocene derivatives (L1-L4)

Three new aromatic substituted ferrocene derivatives were synthesized (**L1-L4**) in a good yield by reacting an equimolar amount of the phenyl-, nitro, sulfonyl- and **L4** with chloro– substituted aminophenol (0.5 mmol) and ferrocenecarboxaldehyde (0.5 mmol) using ethanol as a solvent as shown in Scheme. 1. The structure and composition of the ferrocene compounds were confirmed by ^{1}HNMR, mass spectrometry, FT-IR and UV–Vis spectroscopy. The structure of compound L4 was also characterized by single-crystal x-ray diffraction.

FT-IR spectra of **L1-L4** were recorded in the frequency range of 4000–400 cm^{-1} which showed all expected characteristic peaks. Imine function (C = N sp^2 stretching bands) of all compounds appeared as strong signals at 1596 (**L1**), 1592 (**L2**), 1639 (**L3**), and 1582 (**L4**) in the IR spectra.

The bands at 3100–2800 cm^{-1} can be attributed to aromatic ν(C – H). Band at 1101, 1080 cm^{-1} (**L1**), 1104, 1073cm^{-1} (**L2**), 1102, 1071 (**L3**) and 1105, 1084 cm^{-1} (**L4**) are observed for ferrocene moiety. A Cp ν(C–H) stretching vibration can be seen at 468, 488 cm^{-1} (**L1**), 471, 493.cm^{-1} (**L2**), 461, 566 cm^{-1}(**L3**) and 471, 497 cm^{-1} (**L4**).

The ^{1}H NMR and ^{13}C NMR spectra of synthesized compounds (**L1-L4**) were recorded in DMSO–d_6 at room temperature. In all the ^{1}H NMR spectra of **L1-L3**, the characteristic singlet of the azomethine (CH=N) proton that confirmed the formation of Schiff base has appeared at 8.49, 8.59, and 8.61 ppm respectively. Protons of the unsubstituted cyclopentadienyl ring η^5-C_5H_5 of **L1-L3** has appeared at 4.32, 4.30, and 4.29 ppm respectively. The signals of the substituted cyclopentadienyl ring η^4-C_5H_4 were observed at 4.69 and 4.82 ppm in **L1**, 4.68 and 4.91 ppm in **L2,** and 4.47 and 4.80 ppm in case of **L3**. The signals of aromatic protons of **L1** was seen as four singlets at 6.45, 6.54, 6.70, and 6.89 ppm whereas three multiplets for aromatic protons appeared at 7.24, 7.37 and 7.50 ppm. In the case of ligand **L2**, two doublets with coupling constant of 8.5 Hz were observed at 6.75, 7.37 ppm, and a singlet of

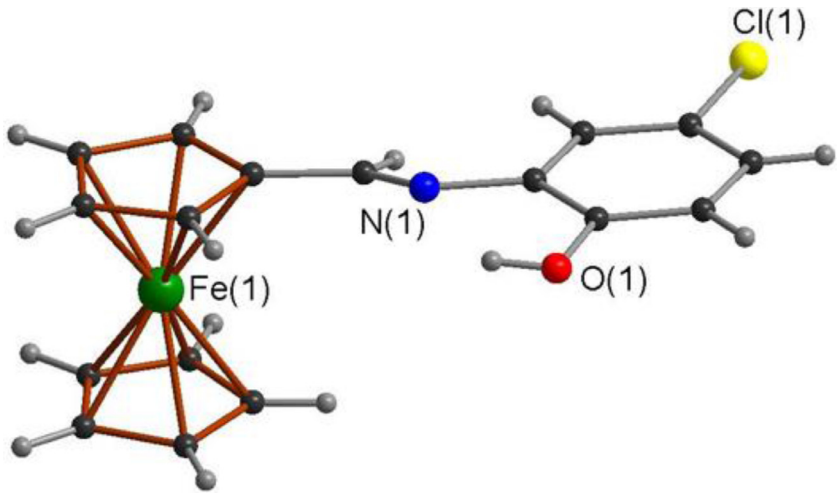

Fig. 1. Molecular structure of ferrocenyl schiff base (L4).

Table 2
Selected bond distances and bond angles of L4.

Bond length (Å)		Bond angles(°)	
C(6)-C(11)	1.438(5)	C(6)-C(11)-N(1)	123.8(4)
C(11)-N(1)	1.275(5)	C(11)-N(1)-C(12)	120.0(3)
C(12)-N(1)	1.425(5)	N(1)-C(12)-C(17)	124.8(3)
C(16)-Cl(1)	1.731(5)	N(1)-C(12)-C(13)	116.8(3)
C(13)-O(1)	1.356(5)	O(1)-C(13)-C(12)	122.7(3)
Fe-C[a]	1.382(6)	Cl(1)-C(16)-C(15)	119.4(4)
C-C[a]	1.382(6)	Cl(1)-C(16)-C(17)	119.7(3)

one proton was recorded at 7.46 ppm. Protons of ligands **L3** were seen as two doublets that appeared at 6.88 and 7.40 ppm with a coupling constant of 8.6 Hz and a singlet at 7.53 ppm. The broad singlets for the phenolic OH group proton in **L1-L3** are at 9.31, 9.36 and 9.34 ppm respectively.

The ^{13}C NMR spectrum of **L1-L3** displayed signals for C-2 and C-5 at 69.88, 69.87, and 69.91 and 73.53, 73.52 and 73.61 ppm for C-3 and C-4 for substituted cyclopentadienyl ring η^4-C_5H_4. The signals at 69.91, 69.90, and 73.53 ppm were assigned for the unsubstituted cyclopentadienyl ring η^5-C_5H_5, whereas signals at 80.02, 79.88, and 79.87 ppm were assigned for C-1 of the substituted cyclopentadienyl ring η^4-C_5H_5 of **L1-L3** respectively. In ^{13}C NMR spectra of **L1-L3**, the signals appeared at 165.93, 166.85 and 163.83 ppm were assigned to C=N respectively. The signals of the phenyl groups were found in the expected regions at 108.11 to 141.02. The signals of aromatic carbons of **L1-L3** bearing OH groups were resonating at 148.57, 151.13, and 150.06 ppm respectively.

The ligands **L1-L3** were further confirmed by mass spectrometry. The *m/z* ratios of the compounds **L1-L3** measured are 381.09, 351.06, and 382.06 respectively which are in complete agreement with the theoretical structural formula of the Schiff bases.

3.2. Crystal structure of L4

The structure of **L4** was confirmed using single-crystal X-ray crystallography. The structure and labeling scheme is depicted in Fig. 1. Selected bond lengths and angles are presented in Table 2. **L4** crystallized in the centrosymmetric $P2_1/n$ space group. The –C=N– bond length (1.275(6) Å) is consistent with the values reported for related ferrocene Schiff bases of general formula [(η5 -C_2H_5) Fe (η^5-C_2H_5CH=N–C_6H_4(OH)] and [(η^5-C_2H_5) Fe (η^5-C_2H_5C(R)=N(C_6H_4–2-OH)] (R = Me, C_6H_5) [29]. The other bond lengths and angles of the ferrocenyl moiety agree with those reported for most ferrocene derivatives [30] The value of the torsion angle C(6)–C(11)–N(1)–C(12) (177.2°) indicates that the imine adopts the anti-(*E*) form which is good agreement with known Schiff bases derived from ferrocene [31]. Also, the advantage of the anti-(*E*) form is to retain the co-planarity between the donor and acceptor group which is important for the charge transfer process [32].

3.3. Electronic properties

The highest occupied / lowest unoccupied molecular orbitals (HOMOs / LUMOs) of studied compounds were probed at B3LYP/6–31G**(LANL2DZ) level (Fig. 3) and the optimized structure of **L4** is given in figure S2. The spatial scattering of HOMO within dexamethasone was observed at C = O whereas LUMO over side ring of phenanthrene. The intramolecular charge transfer (ICT) was found for keto C = O (HOMO) to the side ring of phenanthrenee (LUMO). In remdesivir, the HOMO was at pyrrolotriazin unit whereas the LUMO at [1,2,4] triazin-7-yl aminopyrrolo [2,1-f] revealing the ICT from HOMO to LUMO. In hydroxychloroquine, ICT was also found from HOMO at amino group of (ethyl)amino]ethanol unit) to LUMO (quinolin) and HOMO → LUMO. In favipiravir, HOMO is primarily at 6-fluoro-3-hydroxypyrazine as well as oxygen of carboxamide moiety while the LUMO is pyrazine-2-carboxamide illuminating ICT from HOMO to LUMO. Similarly, in the synthesized ferrocene derivatives ICT was noticed from HOMOs to LUMOs. The activity of compounds was also strictly associated with the spatial distribution of occupied molecular orbitals enlightening the most credible locations in order that certainly attacked by reactive agents. The FMOs were superimposed considerably thus revealing the particularly reactive nature of the drugs. The energies of FMOs, for example, HOMO (E_{HOMO}), LUMO (E_{LUMO}), as well as HOMO-LUMO energy gaps (E_{gap}) were significant parameters to probe molecular electronic characteristics. The E_{HOMO}, E_{LUMO}, and E_{gap} of recently synthesized ferrocene derivatives along with reference drugs dexamethasone, remdesivir, hydroxychloroquine, and favipiravir are displayed in Table 3. The molecular structures of the reference drugs are given below.

The measurements of global chemical reactivity descriptors (GCRD) are essential considerations to figure out the activity. Herein, the large number of GCRD parameters were estimated including the electrophilicity index (ω), softness (S), electronegativity (χ), chemical potential (μ) as well as chemical hardness (η) with the help of HOMO/LUMO energies.

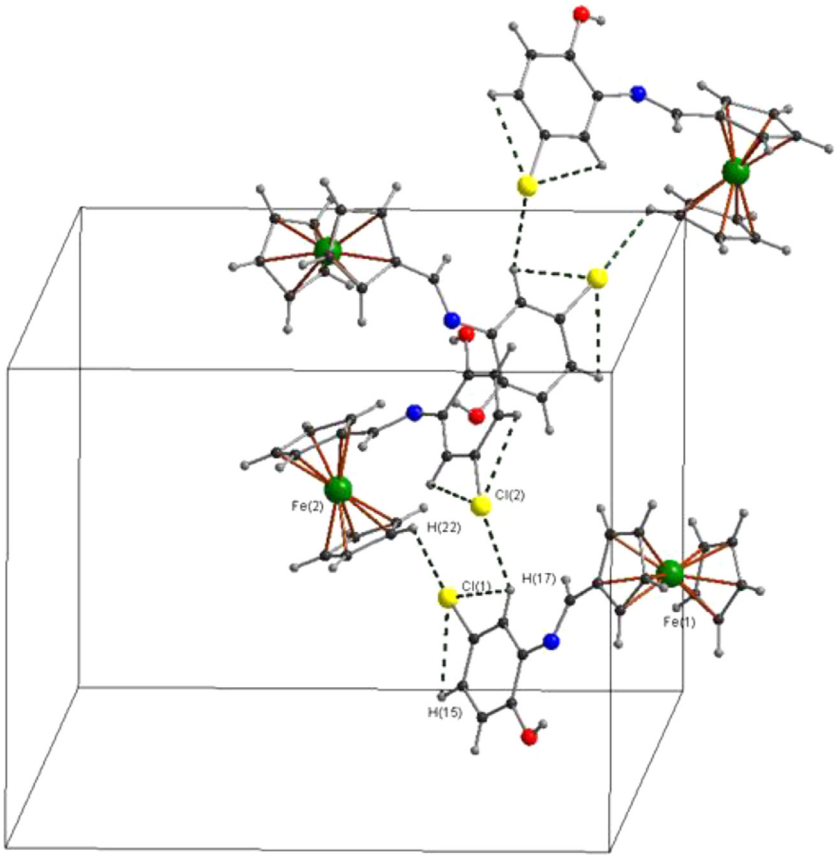

Fig. 2. Compound L4 showing the formation of dimer C–H···Cl interactions.

Table 3
The frontier molecular orbitals (E_{HOMO} and E_{LUMO}), energy gaps (E_{gap}), various molecular descriptors, electron injection energy (EIE), and hole injection energy (HIE) barriers of ferrocene derivatives calculated at B3LYP/6–31G**(LANL2DZ) level.

Parameters	L1	L2	L3	L4	dexamethasone	remdesivir	hydroxyl-chloroquine	Favipiravir
E_{HOMO}	−5.33	−5.89	−5.83	−5.58	−6.22	−6.20	−5.57	−6.98
E_{LUMO}	−1.56	−2.08	−1.90	−1.73	−1.39	−1.36	−1.14	−2.24
E_{gap}	3.77	3.81	3.93	3.85	4.83	4.84	4.43	4.74
IP	5.33	5.89	5.83	5.58	6.22	6.20	5.57	6.98
EA	1.56	2.08	1.90	1.73	1.39	1.36	1.14	2.24
η	1.885	1.905	1.965	1.925	2.41	2.42	2.21	2.37
μ	−3.445	−3.985	−3.865	−3.655	−3.80	−3.78	−3.35	−4.61
S	1.414	1.546	1.483	1.449	1.29	1.28	1.26	1.47
χ	3.445	3.985	3.865	3.655	3.80	3.78	3.35	4.61
ω	3.148	4.168	3.801	3.470	4.428	4.604	4.363	4.609
HIE (Au)	0.23	0.79	0.73	0.48	1.12	1.10	0.47	1.88
EIE (Au)	2.15	1.72	1.82	3.37	3.71	3.74	3.96	2.86
HIE (Al)	1.25	1.81	1.75	1.50	2.14	2.12	1.49	2.90
EIE (Al)	2.52	2.00	2.18	2.35	2.69	2.72	2.94	1.84

An approximation for absolute hardness η was developed [33–35] as given below:

$$\eta = \frac{IP - EA}{2} \quad (1)$$

where *I* is the vertical ionization energy and *A* is vertical electron affinity.

As per Koopmans theorem [36] the ionization energy and electron affinity can be specified through HOMO and LUMO orbital energies as:

$$IP = -E_{HOMO} \quad (2)$$

$$EA = -E_{LUMO} \quad (3)$$

Values of EA and IP of calculated are given in Table 3. The higher energy of HOMO is corresponding to the more reactive molecule in the reactions with electrophiles, while lower LUMO energy is essential for molecular reactions with nucleophiles [37].

Hence, the hardness of any materials corresponds to the gap between the HOMO and LUMO orbitals. If the energy gap of HOMO-LUMO is large then the molecule becomes harder [35].

$$\eta = \frac{1}{2}\ (E_{LUMO} - E_{HOMO}) \quad (4)$$

The electronic chemical potential (μ) of a molecule is calculated by:

$$\mu = -\left(\frac{IP + EA}{2}\right) \quad (5)$$

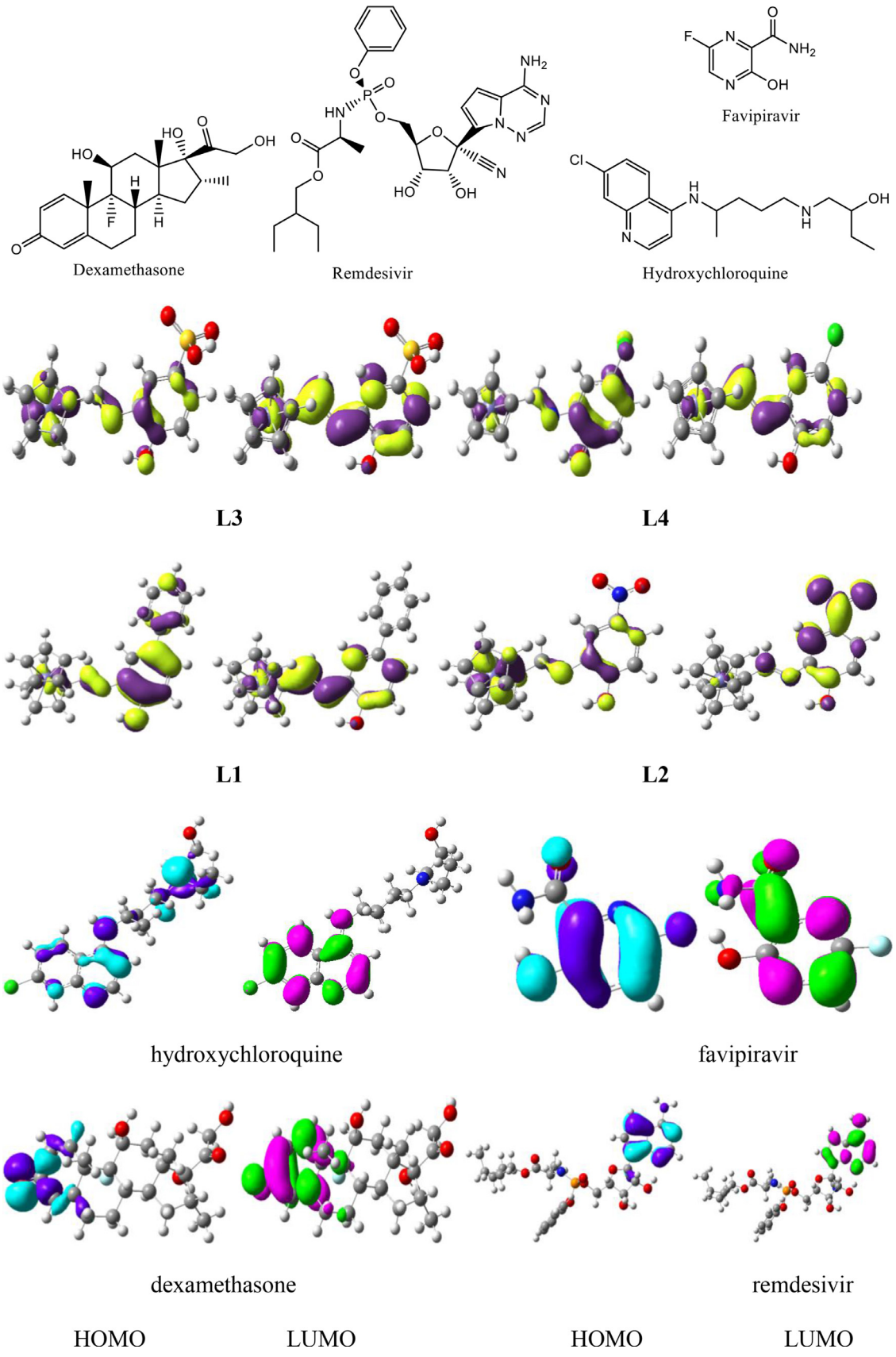

Fig. 3. Ground state charge density of FMOs of Ferrocene derivatives and reference drugs used against COVID (contour value=0.035).

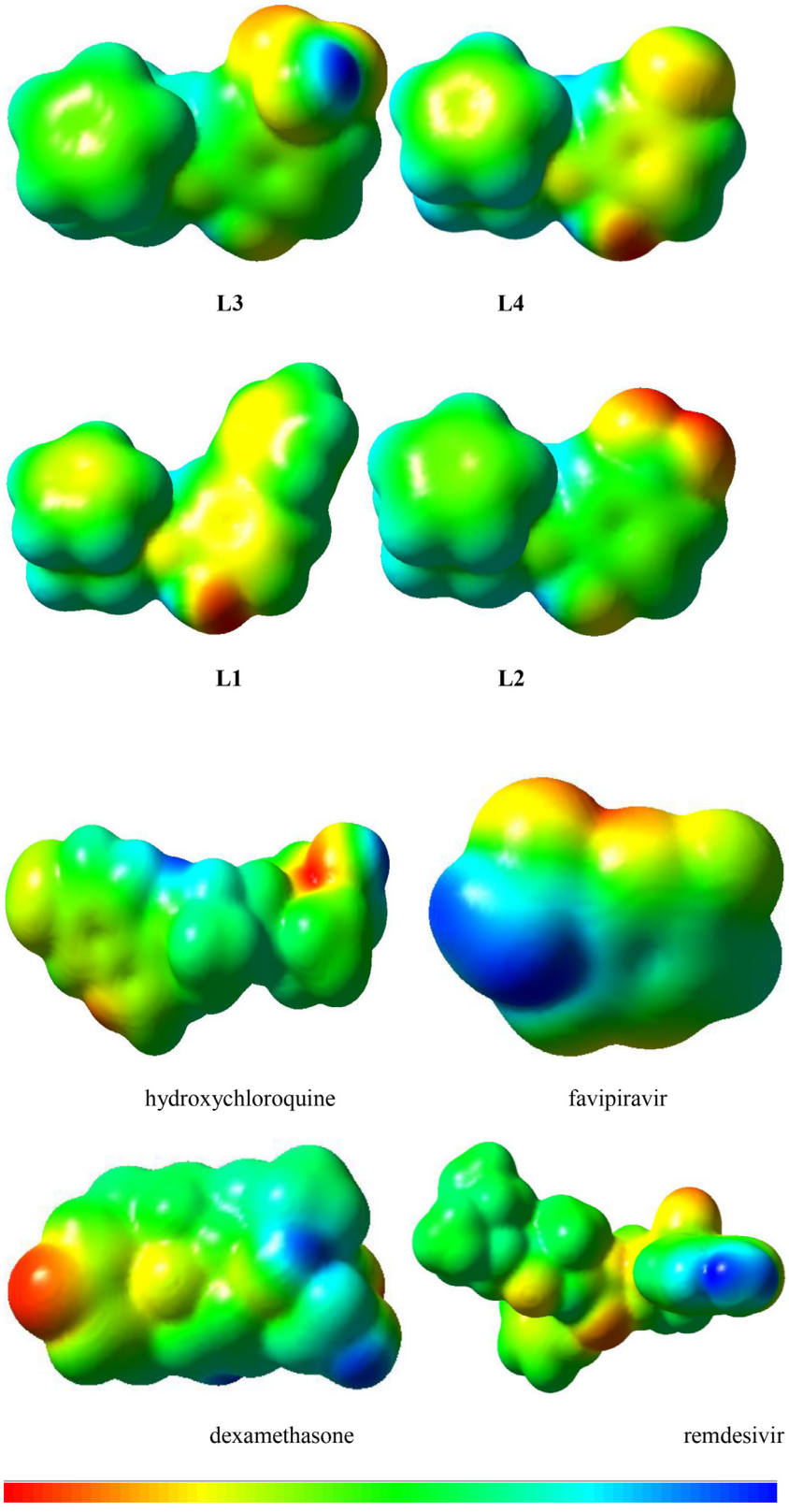

Fig. 4. Molecular electrostatic potential surfaces views of Ferrocene derivatives and reference drugs.

Fig. 5. Crystal structure of the virus main protease in the complex (6LU7) (water molecules and inhibitor N3 are removed for clarity).

The softness of a molecule is calculated by:

$$S = \frac{I}{2\eta} \tag{6}$$

The electronegativity of the molecule is calculated by:

$$\chi = \left(\frac{IP + EA}{2}\right) \tag{7}$$

The electrophilicity index of the molecule is calculated by:

$$\omega = \frac{\mu^2}{2\eta} \tag{8}$$

The η is interconnected to aromaticity and the value of ω represents the stabilization energy for saturated compound by electrons from the exterior environment [38,39]. The value of μ conveys the electronic tendency to run away based on its electronic cloud whereas the η value provides a degree of hindrance of electronic cloud toward deformation. We have previously reported that

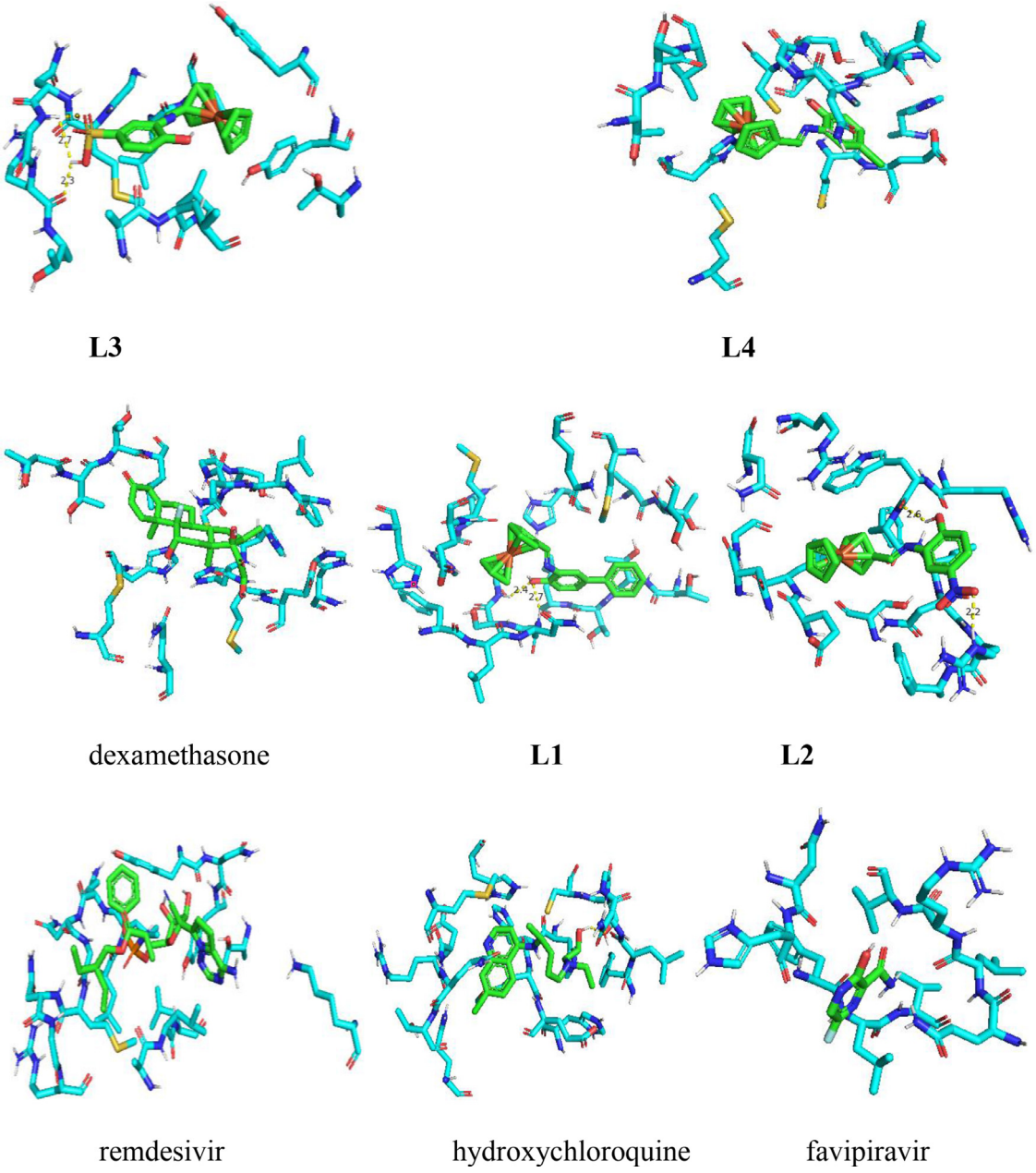

Fig. 6. Docking simulation of the interaction between Ferrocene derivatives and reference drugs (green color) and 6LU7 protein.

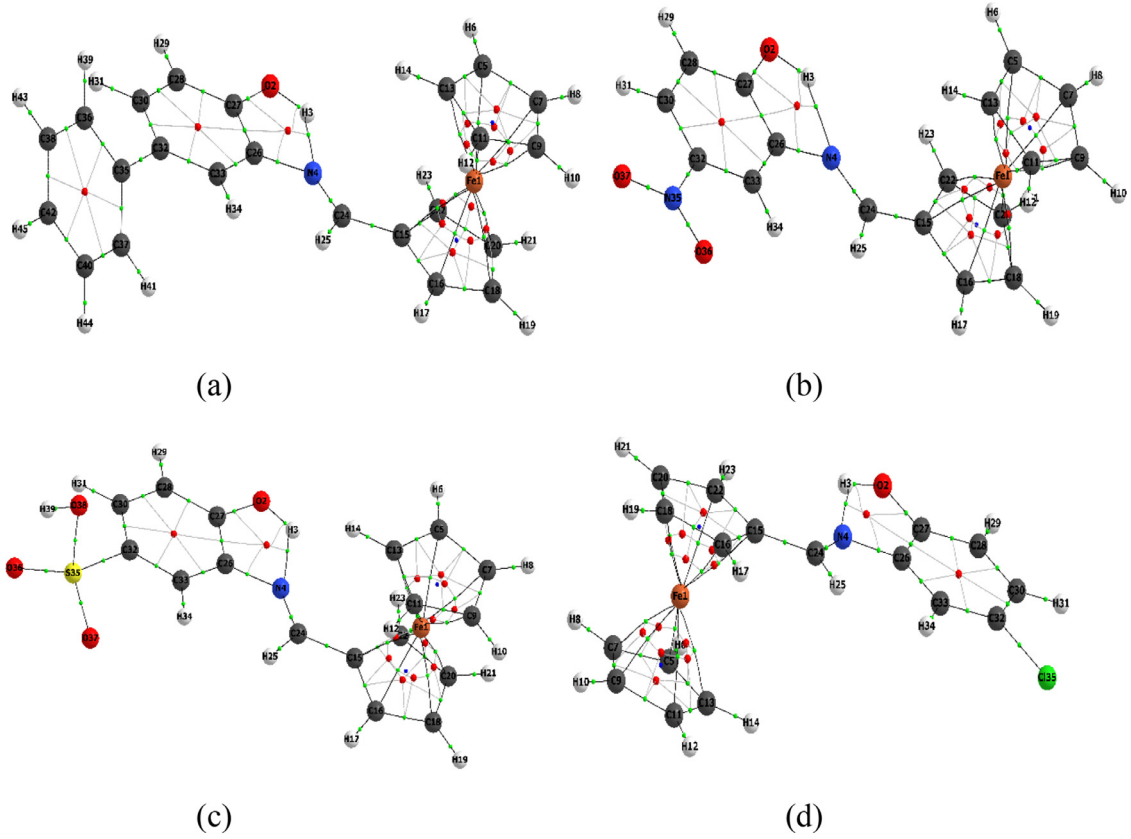

Fig. 7. AIM Molecular graphs of title compounds: green small spheres (BCPs), small red sphere (RCBs), black lines (bond paths), and ash color solid lines (RCP to BCP ring path).

the better radical scavenging ability of a drug was a prerequisite to hinder viral infections [40]. The antioxidant compounds contribute an electron to the free radical and the resulting radical cation should be stable enough to demonstrate better radical scavenging ability in a one-electron transfer mechanism. In this way, the antioxidant ability can be evaluated by ionization potential (IP) and the physical parameter highlighting the electron transfer range can be estimated by IP= $-E_{HOMO}$. It is anticipated that radical scavenging nature might be superior for those compounds which show smaller IP. The results in Table 3 revealed that **L1** have the smallest IP value therefore, it might be a better radical scavenger having good antioxidant ability as compared to the reference drugs (dexamethasone, remdesivir, hydroxychloroquine, and favipiravir).

The hole and electron injection energies (HIE and EIE) of these synthesized ferrocene derivatives were calculated and compared to Al and Au electrodes having work function (W) 4.08 and 5.10 eV respectively. The EIE of ferrocene derivatives were estimated as (eV = $-E_{LUMO} - (-W)$) and HIE as (eV = $-W - (-E_{HOMO})$), see Table 3. The hole and electron injection barriers of ferrocene derivatives were found to be smaller than most of the reference drugs.

3.4. Molecular electrostatic potential

The molecular electrostatic potential (MEP) was measured experimentally by diffraction approaches and calculated computationally to explore the reactivity of various compounds and/or species [41,42]. The MEP is an important feature to understand the reactivity of various species [43]. The MEP mapped for ferrocene derivatives and reference drugs are illustrated in color visualizations in Fig. 3. The red color indicates the higher negative potential regions which are favorable for an electrophilic attack, whereas the blue color identifies the higher positive potential regions promising for nucleophilic attack. The MEP decreases in the order blue > green > yellow > orange > red. The maps of molecular electrostatic potential (MEP) were essential to visualize charged regions within the compounds. The MEP mapped with respect to ferrocene derivatives and reference drugs are shown in color displays in Fig. 4. The red and blue color band identifies negative as well as positive potential areas that would be favorable for electrophilic as well as nucleophilic attack, respectively. In dexamethasone, the negative potential can be seen on O- atoms while positive potential is formed at the H atoms of hydroxyl groups. In remdesivir, negative potential can be seen on oxygen atoms while positive potential at hydrogen atoms of the amino group. In hydroxychloroquine, negative potential can be seen on the oxygen atom of quinolin and oxygen atom of ethanol group while positive potential at hydrogen atoms of hydroxyl and –NH. In favipiravir, negative potential can be seen on the oxygen atoms while positive potential at hydrogen atoms carboxamide moiety. The negative potential can be seen on the O- atom of -OH in **L1**, on the nitro group in **L2**, and oxygen atoms of $-SO_3H$ in **L3**. However, a positive potential is concentrated within hydrogen atoms. The negative potential (red region) on oxygen atoms indicated further the possible sites for the electrophilic attack. Whereas, blue color (positive potential) on hydrogen atoms revealed that these sites would be promising for nucleophilic attack.

4. Molecular docking

The structure of the 6LU7 proteins of SARS-CoV-2 is deposited in the Worldwide Protein Data Bank. The virus core protease crystal structure in the complex (6LU7) without water molecules and inhibitor are shown in Fig. 5. The 6LU7 protein structure was

Table 4
Docking simulation results with Docking Score Energy (DS), sequence between the referenced and ferrocene derivatives and 6LU7 Protein of SARS-CoV-2.

Compounds	BE	Binding sequence
L1	−6.00	GLY143, CYS145
L2	−5.20	TRP218, ARG222
L3	−4.64	ARG222, GLY278, ARG279
L4	−5.01	GLY143
dexamethasone	−6.69	THR26, ASN142, GLU166
remdesivir	−1.43	TYR237, MET276, ASN277, GLY278
hydroxychloroquine	−5.07	LEU141, SER144, HIS163, GLU166
favipiravir	−3.77	GLN74, LEU75, VAL77, VAL68, LEU67, PHE66

Table 5
Topological parameters of the title compounds for selected CPs.

Compound	BCP	ρ(r) (a.u)	$\nabla^2\rho$(r) (a.u)	V(r) (a.u)	G (r) (a.u)	H(r) (a.u)	-G/V	ε
L1	Fe1-C15	0.085	0.282	−0.132	0.101	−0.031	0.767	0.339
	Fe1-C20	0.084	0.272	−0.127	0.097	−0.029	0.768	0.349
	Fe1-C18	0.085	0.271	−0.128	0.098	−0.030	0.765	0.310
	N4-C26	0.261	−0.423	−0.375	0.135	−0.241	0.359	0.033
	C26-C33	0.294	−0.850	−0.423	0.105	−0.318	0.249	0.180
	C15-C22	0.267	−0.716	−0.119	0.102	−0.016	0.862	0.154
	O2-C27	0.266	−0.306	−0.432	0.178	−0.254	0.411	0.007
	C30-H31	0.267	−0.790	−0.285	0.044	−0.241	0.153	0.004
	Fe1-C13	**0.084**	**0.265**	**−0.124**	**0.095**	**−0.029**	**0.767**	**0.353**
	H3-N4	0.035	0.109	−0.035	0.031	−0.004	0.894	0.228
	O2-C27	0.266	−0.306	−0.432	0.178	−0.254	0.411	0.020
L2	Fe1-C15	0.085	0.285	−0.133	0.102	−0.031	0.768	0.337
	Fe1-C20	**0.084**	**0.272**	**−0.126**	**0.097**	**−0.029**	**0.770**	**0.371**
	Fe1-C18	0.084	0.272	−0.127	0.097	−0.030	0.767	0.341
	N4-C26	0.264	−0.439	−0.375	0.133	−0.242	0.354	0.032
	C26-C33	0.299	−0.875	−0.435	0.108	−0.327	0.249	0.179
	C15-C22	0.267	−0.712	−0.363	0.092	−0.270	0.255	0.153
	O2-C27	0.271	−0.321	−0.451	0.185	−0.266	0.411	0.016
	C30-H31	0.271	−0.817	−0.285	0.040	−0.245	0.142	0.000
	H3-N4	0.037	0.111	−0.037	0.032	−0.005	0.875	0.203
	N35-O37	0.369	−0.309	−0.643	0.283	−0.360	0.440	0.068
	O2-H3	0.284	−1.051	−0.389	0.063	−0.326	0.162	0.019
L3	Fe1-C15	0.085	0.286	−0.133	0.102	−0.031	0.768	0.340
	Fe1-C20	0.084	0.272	−0.126	0.097	−0.029	0.770	0.367
	Fe1-C18	0.084	0.271	−0.127	0.097	−0.030	0.767	0.337
	Fe1-C13	**0.083**	**0.264**	**−0.123**	**0.095**	**−0.029**	**0.768**	**0.371**
	N4-C26	0.264	−0.442	−0.377	0.133	−0.243	0.353	0.035
	C26-C33	0.296	−0.862	−0.429	0.107	−0.322	0.249	0.180
	C15-C22	0.267	−0.713	−0.363	0.092	−0.271	0.255	0.153
	O2-C27	0.270	−0.321	−0.446	0.183	−0.263	0.410	0.012
	S35-O38	0.157	0.056	−0.173	0.094	−0.080	0.540	0.083
	C32-S35	0.165	−0.196	−0.157	0.054	−0.103	0.343	0.064
	S35-O37	0.217	−0.242	−0.320	0.130	−0.190	0.405	0.008
	C30-H31	0.269	−0.806	−0.282	0.040	−0.242	0.143	0.003
	H3-N4	0.037	0.110	−0.036	0.032	−0.004	0.882	0.212
	S35-O38	0.157	0.056	−0.173	0.094	−0.080	0.540	0.083
	O38-H39	0.294	−1.007	−0.380	0.064	−0.316	0.169	0.026
	O2-H3	0.285	−1.061	−0.391	0.063	−0.328	0.161	0.019
L4	Fe1-C15	0.085	0.283	−0.132	0.102	−0.031	0.768	0.339
	Fe1-C20	**0.084**	**0.272**	**−0.126**	**0.097**	**−0.029**	**0.769**	**0.362**
	Fe1-C18	0.084	0.271	−0.127	0.098	−0.030	0.766	0.327
	N4-C26	0.264	−0.436	−0.378	0.134	−0.243	0.356	0.036
	C26-C33	0.291	−0.837	−0.417	0.104	−0.313	0.249	0.186
	C15-C22	0.267	−0.714	−0.119	0.103	−0.016	0.862	0.154
	O2-C27	0.267	−0.310	−0.432	0.177	−0.255	0.410	0.003
	C30-H31	0.269	−0.802	−0.284	0.042	−0.242	0.148	0.008
	H3-N4	0.035	0.109	0.099	0.031	0.130	−0.308	0.237
	C32-Cl35	0.143	−0.094	−0.131	0.054	−0.077	0.411	0.040
	O2-C27	0.267	−0.310	−0.432	0.177	−0.255	0.410	0.003
	O2-H3	0.288	−1.077	−0.396	0.064	−0.333	0.160	0.020

refined using Autodock and a model outlining the docking analysis of molecules along with standards drugs. The binding energy values between ligands and protein (active sites in the title compounds along with amino acids) are displayed in Table 4 and Fig. 5. The binding energy values between ligands and 6LU7 proteins of SARS-CoV-2 (active sites in the title compounds and 6LU7 proteins of the SARS-CoV-2) were given in Table 4 and Fig. 6. In **L1**, the hydrogen bonding between H of ligand to O—H of CYS145 was found to be 2.40 Å, and H of GLY143 and O of ligand was 2.70 Å. Hydrogen bonding between keto O of TRP218 to H—O of ligand was found to be 2.60 Å and hydrogen bonding between H of ARG222 and O—N—O of ligand was found to be 2.20 Å in **L2**. In Compound

L3, hydrogen bonding between keto O of ARG279 and HSO_3 of ligand was found to be 2.70 Å, hydrogen bonding between keto O of GLY278 and HSO_3 of ligand was found 2.30. The docking results for **L1-L4** highlighted that the **L1** might have better anti-oxidant and anti-COVID19 ability than other counterparts. The computation outcome indicates that **L1** exhibit better inhibition against SARS-CoV-2 as compared to the reference drugs. This finding leads to further exploration of **L1** and its potential application in the prevention and treatment of SARS-CoV-2.

5. QTAIM analysis

In this present work, the electron density $\rho(r)$, the second derivative electron density of Laplacian electron density $\nabla^2\rho(r)$, potential energy density $V(r)$, local energy density $H(r)$, kinetic energy density $G(r)$, the ratio of –(G/V) and ellipticity (ε) [44,45] of the title compounds (L1-L4) for selected BCPs are listed in Table 4. The AIM molecular maps of the L1-L4 are shown in Fig. 7(a), (b), (c) and (d) exhibit respectively. In the present case, BCPs at all Iron-Carbon (Fe-C) values for all compounds of $\rho(r)$ and $\nabla^2\rho(r)$ are indicates that closed-shell interactions. The highest $\rho(r)$ (0.085a.u for all) values with corresponding positive $\nabla^2\rho(r)$ (0.282, 0.285, 0.286 and 0.283 a.u) values were found at Fe1-C15 for L1-L4, respectively. Also, one intramolecular hydrogen bond at H3-N4 was confirmed in all selected compounds by the values of $\rho(r)$, and $\nabla^2\rho(r)$ (e.g. L4, $\rho(r) = 0.035$ a.u, & $\nabla^2\rho(r) = 0.109$ a.u). In the Table 4, the computed value of $\rho(r)$ 0.143 to 0.299 a.u., and corresponding negative values of $\nabla^2\rho(r)$, of BCPs, represent that the shared interactions of covalent bonds.

The asymmetry of electron density distribution is described by bond ellipticity (ε) [46,47]. The highest ε values were found at Fe-C13, Fe1-C20, Fe1-C13 and Fe1-C20 of respective compounds (L1-L4), showing a highly asymmetric electron density at the BCPs.

6. Conclusion

Since COVID-19 has acquired pandemic status and new variants of corona require the attention of academicians to discover a possible safe and effective drug to ameliorate its effects worldwide. Due to various biological applications of ferrocene derivatives, their structural properties like lipophilicity of ferrocenyl groups, redox potential activation energy, low toxicity, strong antigenic response and oral administration make them potential candidates against COVID-19. In the present study, four new ferrocene derivatives were successfully synthesized and characterized by NMR spectroscopy, mass spectrometry, and single-crystal x-ray diffraction technique. A theoretical insight on synthesized ferrocene derivatives was accomplished by docking score, frontier molecular orbitals energies, active sites, and molecular descriptors which were further compared with drugs being currently used against COVID-19, *i.e.*, dexamethasone, hydroxychloroquine, favipiravir, and remdesivir. Moreover, the inhibitions of ferrocene derivatives were recorded on the core protease (6LU7) protein of SARS-CoV-2 and the effect of substituents on the anti-COVID activity through the molecular docking approach. The docking results for **L1-L4** highlighted that the **L1** might have better anti-oxidant and anti-COVID19 ability than other currently used drugs. The computational outcome indicated that such compounds have powerful 6LU7 inhibition of SARS-CoV-2. These findings could be helpful for further exploration of new ferrocene derivatives and their potential applications in the prevention and treatment of SARS-CoV-2. The experimental investigation of biological and anti-Covid activity of these compounds is in progress and will be published separately.

CRediT authorship contribution statement

Ghulam Abbas: Conceptualization, Methodology, writing and reviewing **Ahmad Irfan**: Computational studies and reviewing, **Ishtiaq Ahmed**: spectroscopic analysis, **Firas Khalil Al-Zeidaneen**: Uv-Vis and Mass spectrometry. **S. Muthu**: Molecular docking, **Olaf Fuhr**: Single crystal X-ray diffraction and **Renjith Thomas** Molecular docking and reviewing.

Declaration of Competing Interest

The authors declare that they have no known competing financial interests or personal relationships that could have appeared to influence the work reported in this paper.

Acknowledgements

The author G Abbas acknowledge Prof Annie K. Powell for Providing lab. facilities at KIT Karlsruhe Germany and A. Irfan to the Deanship of Scientific Research at King Khalid University, Saudi Arabia for funding through research groups program (R.G.P.1/110/42).

Supplementary materials

Supplementary material associated with this article can be found, in the online version, at doi:10.1016/j.molstruc.2021.132242.

References

[1] V. Coronaviridae, Study group of the international committee on taxonomy of, the species severe acute respiratory syndrome-related coronavirus: classifying 2019-nCoV and naming it SARS-CoV-2, Nat Microbiol 5 (2020) 536–544 10.1038/s41564-020-0695-z.
[2] W.C.J. Culp, Coronavirus disease 2019: in-home isolation room construction, A&A Pract. 14 (2020) e0121810.1213/xaa.0000000000001218.
[3] W.H. Organization, COVID-19 Weekly Epidemiological Update, 5 Oct. 2021, (2021)
[4] C. Wang, P.W. Horby, F.G. Hayden, G.F. Gao, A novel coronavirus outbreak of global health concern, The Lancet 395 (2020) 470–473, doi:10.1016/S0140-6736(20)30185-9.
[5] S.A. Lone, A. Ahmad, COVID-19 pandemic–an African perspective, Emerg. Microbes Infect. 9 (2020) 1300–1308.
[6] J. Mellet, M. Pepper, A COVID-19 vaccine: big strides come with big challenges, Vaccines (Basel) 9 (2021) 39 2021, doi:10.3390/vaccines9010039.
[7] M. Patra, G. Gasser, The medicinal chemistry of ferrocene and its derivatives, Nat. Rev. Chem. 1 (2017) 1–12, doi:10.1038/s41570-017-0066.
[8] R.A. Yeary, Chronic toxicity of dicyclopentadienyliron (ferrocene) in dogs, Toxicol. Appl. Pharmacol. 15 (1969) 666–676, doi:10.1016/0041-008X(69)90067-2.
[9] G. Jaouen, Bioorganometallics: Biomolecules, Labeling, Medicine, John Wiley & Sons, 2006 3527607110.
[10] V.J. Fiorina, R.J. Dubois, S. Brynes, Ferrocenyl polyamines as agents for the chemoimmunotherapy of cancer, J. Med. Chem. 21 (1978) 393–395, doi:10.1021/jm00202a016.
[11] T. Gill, L. Mann, Studies on synthetic polypeptide antigens: XV. the immunochemical properties of ferrocenyl-poly Glu58Lys36Tyr6 (No. 2) conjugates, J. Immunol. 96 (1966) 906–912.
[12] J. Chadwick, A.E. Mercer, B.K. Park, R. Cosstick, P.M. O'Neill, Synthesis and biological evaluation of extraordinarily potent C-10 carba artemisinin dimers against P. falciparum malaria parasites and HL-60 cancer cells, Bioorg. Med. Chem. 17 (2009) 1325–1338 https://doi.org/10.1016/j.bmc.2008.12.017.
[13] G.H. Posner, A.J. McRiner, I.-.H. Paik, S. Sur, K. Borstnik, S. Xie, T.A. Shapiro, A. Alagbala, B. Foster, Anticancer and antimalarial efficacy and safety of artemisinin-derived trioxane dimers in rodents, J. Med. Chem. 47 (2004) 1299–1301 https://doi.org/10.1021/jm0303711.
[14] C. Reiter, T. Fröhlich, M. Zeino, M. Marschall, H. Bahsi, M. Leidenberger, O. Friedrich, B. Kappes, F. Hampel, T. Efferth, New efficient artemisinin derived agents against human leukemia cells, human cytomegalovirus and Plasmodium falciparum: 2nd generation 1, 2, 4-trioxane-ferrocene hybrids, Eur J Med Chem 97 (2015) 164–172, doi:10.1016/j.ejmech.2015.04.053.
[15] G.M. Sheldrick, SHELXT–Integrated space-group and crystal-structure determination, Acta Crystallograph. Section A 71 (2015) 3–8.
[16] A. Irfan, F.K. Al-Zeidaneen, I. Ahmed, A.G. Al-Sehemi, M.A. Assiri, S. Ullah, G. Abbas, Synthesis, characterization and quantum chemical study of optoelectronic nature of ferrocene derivatives, Bull. Mater. Sci. 43 (2020) 1–8, doi:10.1007/s12034-019-1992-0.

[17] E.R. Elsharkawy, F. Almalki, T.B. Hadda, V. Rastija, H. Lafridi, H. Zgou, DFT calculations and POM analyses of cytotoxicity of some flavonoids from aerial parts of Cupressus sempervirens: docking and identification of pharmacophore sites, Bioorg. Chem. 100 (2020), doi:10.1016/j.bioorg.2020.103850.
[18] A. Irfan, A.R. Chaudhry, A.G. Al-Sehemi, Electron donating effect of amine groups on charge transfer and photophysical properties of 1, 3-diphenyl-1H-pyrazolo [3, 4-b] quinolone at molecular and solid state bulk levels, Optik (Stuttg) 208 (2020), doi:10.1016/j.ijleo.2019.164009.
[19] A. Irfan, M. Imran, A.G. Al-Sehemi, M.A. Assiri, A. Hussain, N. Khalid, S. Ullah, G. Abbas, Quantum chemical, experimental exploration of biological activity and inhibitory potential of new cytotoxic kochiosides from Kochia prostrata (L.) Schrad, J. Theor. Comput. Chem. 19 (2020) 2050012.
[20] R.-.Y. Jin, T. Tang, S. Zhou, X. Long, H. Guo, J. Zhou, H. Yan, Z. Li, Z.-.Y. Zuo, H.-.L. Xie, Design, synthesis, antitumor activity and theoretical calculation of novel PI3Ka inhibitors, Bioorg. Chem. 98 (2020), doi:10.1016/j.bioorg.2020.103737.
[21] G. Demirtaş, N. Dege, E. Ağar, S. Şahin, The Crystallographic, Spectroscopic and Theoretical Studies on (E)-2-[((4-*fluorophenyl*) *imino*) *methyl*]-4-nitrophenol and (E)-2-[((3-*fluorophenyl*) *imino*) *methyl*]-4-nitrophenol Compounds, Iranian J. Chem. Chem. Eng. (IJCCE) 37 (2018) 55–65.
[22] D. Mikulski, K. Eder, M. Molski, Quantum-chemical study on relationship between structure and antioxidant properties of hepatoprotective compounds occurring in Cynara scolymus and Silybum marianum, J. Theor. Comput. Chem. 13 (2014), doi:10.1142/S0219633614500047.
[23] M. Najafi, S.A.R. Naqvi, Theoretical study of the substituent effect on the hydrogen atom transfer mechanism of the irigenin derivatives antioxidant action, J. Theor. Comput. Chem. 13 (2014), doi:10.1142/S0219633614500102.
[24] K. Sadasivam, R. Jayaprakasam, R. Kumaresan, A DFT study on the role of different OH groups in the radical scavenging process, J. Theor. Comput. Chem. 11 (2012) 871–893 https://doi.org/10.1142/S0219633612500599.
[25] I. Warad, M. Al-Nuri, O. Ali, I.M. Abu-Reidah, A. Barakat, T. Ben Hadda, A. Zarrouk, S. Radi, R. Touzani, H. Elmsellem, Synthesis, physico-chemical, hirschfield surface and DFT/B3LYP calculation of two new hexahydropyrimidine heterocyclic compounds, (2019) http://hdl.handle.net/10576/14835
[26] A. Irfan, Comparison of mono-and di-substituted triphenylamine and carbazole based sensitizers@(TiO2) 38 cluster for dye-sensitized solar cells applications, Comput. Theor. Chem. 1159 (2019) 1–6, doi:10.1142/S0219633620500121.
[27] A. Mahmood, A. Irfan, Effect of fluorination on exciton binding energy and electronic coupling in small molecule acceptors for organic solar cells, Comput. Theor. Chem. 1179 (2020) 112797, doi:10.1016/j.comptc.2020.112797.
[28] M. Frisch, G. Trucks, H. Schlegel, G. Scuseria, M. Robb, J. Cheeseman, G. Scalmani, V. Barone, G. Petersson, H. Nakatsuji, Gaussian 16, Gaussian, Inc, Wallingford, CT, 2016.
[29] C. Lopez, R. Bosque, S. Pérez, A. Roig, E. Molins, X. Solans, M. Font-Bardía, Relationships between 57Fe NMR, Mössbauer parameters, electrochemical properties and the structures of ferrocenylketimines, J. Organomet. Chem. 691 (2006) 475–484, doi:10.1016/j.jorganchem.2005.09.020.
[30] C. Imrie, P. Kleyi, V.O. Nyamori, T.I. Gerber, D.C. Levendis, J. Look, Further solvent-free reactions of ferrocenylaldehydes: synthesis of 1, 1′-ferrocenyldiimines and ferrocenylacrylonitriles, J. Organomet. Chem. 692 (2007) 3443–3453, doi:10.1016/j.jorganchem.2007.04.011.
[31] M. Benito, C. López, X. Solans, M. Font-Bardıá, Palladium (II) compounds with planar chirality. X-Ray crystal structures of (+)-(R)-[{(η5-C5H4)–CH N–CH (Me)–C10H7} Fe (η5-C5H5)] and (+)-(Rp, R)-[Pd {[(Et–C C–Et) 2 (η5-C5H3)–CH N–CH (Me)–C10H7] Fe (η5-C5H5)} Cl], Tetrahedron: Asymmetry 9 (1998) 4219–4238, doi:10.1016/S0957-4166(98)00437-6.
[32] A. Houlton, J.R. Miller, J. Silver, N. Jassim, M.J. Ahmet, T.L. Axon, D. Bloor, G.H. Cross, Molecular materials for non-linear optics. Second harmonic generation and the crystal and molecular structure of the 4-nitrophenylimine of ferrocenecarboxaldehyde, Inorganica Chim Acta 205 (1993) 67–70 https://doi.org/10.1016/S0020-1693(00)87356-9.
[33] R.G. Parr, P.K. Chattaraj, Principle of maximum hardness, J. Am. Chem. Soc. 113 (1991) 1854–1855 https://doi.org/10.1021/ja00005a072.
[34] R.G. Parr, R.G. Pearson, Absolute hardness: companion parameter to absolute electronegativity, J. Am. Chem. Soc. 105 (1983) 7512–7516 https://doi.org/10.1021/ja00364a005.
[35] R.G. Pearson, Absolute electronegativity and absolute hardness of Lewis acids and bases, J. Am. Chem. Soc. 107 (1985) 6801–6806, doi:10.1021/ja00310a009.
[36] T. Koopmans, Ordering of wave functions and eigenenergies to the individual electrons of an atom, Physica 1 (1933) 104–113, doi:10.1016/S0031-8914(34)90011-2.
[37] A. Rauk, Orbital Interaction Theory of Organic Chemistry, John Wiley & Sons20040471461849.
[38] P. Geerlings, F. De Proft, W. Langenaeker, Conceptual density functional theory, Chem. Rev. 103 (2003) 1793–1874 https://doi.org/10.1021/cr990029p.
[39] A. Vektariene, G. Vektaris, J. Svoboda, A theoretical approach to the nucleophilic behavior of benzofused thieno [3, 2-b] furans using DFT and HF based reactivity descriptors, Arkivoc, (2009) http://dx.doi.org/10.3998/ark.5550190.0010.730
[40] T. Akaike, Role of free radicals in viral pathogenesis and mutation, Rev. Med. Virol. 11 (2001) 87–101, doi:10.1002/rmv.303.
[41] P. Politzer, D.G. Truhlar, Chemical Applications of Atomic and Molecular Electrostatic potentials: reactivity, structure, scattering, and Energetics of organic, inorganic, and Biological Systems, Springer Science & Business Media2013147579634X.
[42] R.F. Stewart, On the mapping of electrostatic properties from Bragg diffraction data, Chem Phys Lett 65 (1979) 335–342, doi:10.1016/0009-2614(79)87077-3.
[43] J.S. Murray, P. Politzer, The electrostatic potential: an overview, Wiley Interdisc. Rev. 1 (2011) 153–163, doi:10.1002/wcms.19.
[44] K. Sangeetha, S. Rajina, M. Marchewka, J. Binoy, The study of inter and intramolecular hydrogen bonds of NLO crystal melaminium hydrogen malonate using DFT simulation, AIM analysis and Hirshfeld surface analysis, Mater. Today 25 (2020) 307–315.
[45] P. Srinivasan, S. Asthana, R.B. Pawar, P. Kumaradhas, A theoretical charge density study on nitrogen-rich 4, 4′, 5, 5′-tetranitro-2, 2′-bi-1H-imidazole (TNBI) energetic molecule, Struct. Chem., 22 (2011) 1213–1220.
[46] S.G. Neogi, A. Das, P. Chaudhury, Investigation of plausible mechanistic pathways in hydrogenation of η 5-(C 5 H 5) 2 Ta (H)= CH 2: an analysis using DFT and AIM techniques, J. Mol. Model 20 (2014) 1–7.
[47] G.G. Sheeba, D. Usha, M. Amalanathan, M.S.M. Mary, Identification of structure activity relation of a synthetic drug 2, 6-pyridine dicarbonitrile using experimental and theoretical investigation, Volume XVI, Issue XI, November 2020, page 89-113.